Chemistry–A European Journal

Research Article
doi.org/10.1002/chem.202303374

Chemistry Europe
European Chemical Societies Publishing

www.chemeurj.org

Dynamic and Assembly Characteristics of Deep-Cavity Basket Acting as a Host for Inclusion Complexation of Mitoxantrone in Biotic and Abiotic Systems

Radoslav Z. Pavlović,[a, b] Tyler J. Finnegan,[a] Anna Metlushko,[b] Alexandar L. Hansen,[c] Christopher A. Waudby,[d] Xiuze Wang,[a] Nicole Hoefer,[e] David W. McComb,[e] Aleksandar Pavić,[f] Nikola Plackić,[f] Jovana Novaković,[g] Jovana Bradić,[g] Nevena Jeremić,[g] Vladimir Jakovljević,[g] Biljana Šmit,[h] Sanja Matić,[h] Matias A. Alvarez-Saavedra,[b] Ivan Čapo,[i] Curtis E. Moore,[a] Samuel I. Stupp,[b] and Jovica D. Badjić*[a]

We describe the preparation, dynamic, assembly characteristics of vase-shaped basket $\mathbf{1}^{3-}$ along with its ability to form an inclusion complex with anticancer drug mitoxantrone in abiotic and biotic systems. This novel cavitand has a deep nonpolar pocket consisting of three naphthalimide sides fused to a bicyclic platform at the bottom while carrying polar glycines at the top. The results of ^{1}H Nuclear Magnetic Resonance (NMR), ^{1}H NMR Chemical Exchange Saturation Transfer (CEST), Calorimetry, Hybrid Replica Exchange Molecular Dynamics (REMD), and Microcrystal Electron Diffraction (MicroED) measurements are in line with **1** forming dimer $[\mathbf{1}_2]^{6-}$, to be in equilibrium with monomers $\mathbf{1}_{(R)}^{3-}$ (relaxed) and $\mathbf{1}_{(S)}^{3-}$ (squeezed). Through simultaneous line-shape analysis of ^{1}H NMR data, kinetic and thermodynamic parameters characterizing these equilibria were quantified. Basket $\mathbf{1}_{(R)}^{3-}$ includes anticancer drug mitoxantrone ($\mathbf{MTO}^{2+}$) in its pocket to give stable binary complex $[\mathbf{MTO}\subset\mathbf{1}]^-$ (K_d = 2.1 μM) that can be precipitated in vitro with UV light or pH as stimuli. Both in vitro and in vivo studies showed that the basket is nontoxic, while at a higher proportion with respect to MTO it reduced its cytotoxicity in vitro. With well-characterized internal dynamics and dimerization, the ability to include mitoxantrone, and biocompatibility, the stage is set to develop sequestering agents from deep-cavity baskets.

[a] *R. Z. Pavlović, T. J. Finnegan, X. Wang, Dr. C. E. Moore, Prof. J. D. Badjić*
Department of Chemistry & Biochemistry
The Ohio State University
1100 W. 18th Avenue, Columbus, OH 43210 (USA)
E-mail: badjic.1@osu.edu

[b] *R. Z. Pavlović, A. Metlushko, M. A. Alvarez-Saavedra, Prof. S. I. Stupp*
Department of Chemistry
Northwestern University
Evanston, IL 60208 (USA)
and
Simpson Querrey Institute for BioNanotechnology
Northwestern University, Chicago, IL 60611(USA)
and
Department of Medicine
Northwestern University
Chicago, IL 60611 (USA)
and
Department of Materials Science and Engineering
Northwestern University
Chicago, IL 60208 (USA)
and
Department of Biomedical Engineering
Northwestern University
Chicago, IL 60208 (USA).

[c] *Dr. A. L. Hansen*
Campus Chemical Instrument Center
The Ohio State University
Columbus, OH 43210 (USA)

[d] *Dr. C. A. Waudby*
School of Pharmacy
University College London
London, WC1N 1AX (UK)

[e] *Dr. N. Hoefer, Prof. D. W. McComb*
Center for Electron Microscopy and Analysis
The Ohio State University
Columbus, OH 43210 (USA)

[f] *Prof. A. Pavić, N. Plackić*
Institute of Molecular Genetics and Genetic Engineering
University of Belgrade
11000 Belgrade (Serbia)

[g] *J. Novaković, J. Bradić, Prof. N. Jeremić, Prof. V. Jakovljević*
Department of Pharmacy
Faculty of Medical Sciences
University of Kragujevac
Kragujevac (Serbia)
and
Center for Excellence for Redox Balance Research in Cardiovascular and Metabolic Disorders
Kragujevac (Serbia)

[h] *Prof. B. Šmit, S. Matić*
University of Kragujevac
Institute for Information Technologies
Department of Science
Kragujevac (Serbia).

[i] *Prof. I. Čapo*
Department of Histology and Embryology
Medical Faculty of Novi Sad
Novi Sad (Serbia)

Supporting information for this article is available on the WWW under https://doi.org/10.1002/chem.202303374

Introduction

Accidental and intentional poisonings (e.g., drugs, pesticides, micropollutants, etc.) are on the rise in both developed and undeveloped nations,[1] with only a handful of antidotes available to reverse the effects of poisoning.[2] With the lack of suitable therapy,[2a,3] a need to discover novel antidotes has been acknowledged by both academic and industrial labs.[4] That is to say, self-assembled structures (intravenous lipid emulsions, liposomes, etc.),[5] nanoparticles,[6] dendrimers,[7] MOFs,[8] antibodies,[9] enzymes,[10] and abiotic receptors[4b,11] have been probed to, via encapsulation, lower the active concentration of toxic substances in blood and tissues with the resulting innocuous structures directed into kidneys or liver for further disposal.[12] With relevance to our study, Bridion (Merck, 2012) was introduced as an effective sequester of neuromuscular relaxant rocuronium to help postoperative recovery of patients. Bridion is a derivative of the γ-cyclodextrin cavitand[13] capable of encapsulating rocuronium, reducing its active concentration in plasma, and therefore accelerating the drug's clearance.

While derivatives of calixarenes, cucurbiturils and pillararenes hold promise as effective and biocompatible sequesters of small molecules and drugs,[4a] there is motivation to introduce other classes of abiotic hosts for addressing intoxication and overdose. Specifically, discovery and optimization of action of sequesters presents many challenges[2c,d] including: (a) development of sufficiently stable and synthetically accessible structures, (b) understanding conformational and assembly characteristics of such hosts, (c) invention of materials with high uptake capacity, selectivity, and affinity toward targeted substances and (d) construction of biocompatible and bioactive structures. In this vein, we decided to examine our recently published methodology[14] for obtaining deep-cavity basket $\mathbf{1}^{3-}$ (Figure 1).

This novel and vase-shaped cavitand has a deep nonpolar pocket (9.5 Å, Figure 1) lined with glycines at its rim for its water solubility. The naphthalimide sides also provide a large aromatic surface, which we posit could form favorable π–π contacts with aromatic guests[15] and should help to stabilize guest binding via the hydrophobic effect.[16] Accordingly, we wondered if anticancer drug mitoxantrone ($\mathbf{MTO}^{2+}$, Figure 1) would occupy the binding pocked of $\mathbf{1}^{3-}$. First, computational studies suggested structural and electronic complementarity of $\mathbf{1}^{3-}$ and $\mathbf{MTO}^{2+}$ (Figure 1).[17] The drug inserts its 7.4 Å long anthraquinone into the basket's pocket to form π–π stacking, C–H···π and salt-bridge contacts. Second, mitoxantrone is an effective DNA intercalator and topoisomerase inhibitor[18] that in some cases causes myelosuppression. It follows that learning about mitoxantrone sequestration[19] can help reduce drug's toxicity and improve chemotherapy.[20] In a broader sense, a great number of anticancer agents possess a flat, aromatic pharmacophore for which deep-cavity baskets may be complementary sequesters. Finally, is deep-cavity basket $\mathbf{1}^{3-}$ cytotoxic or harmful to lab

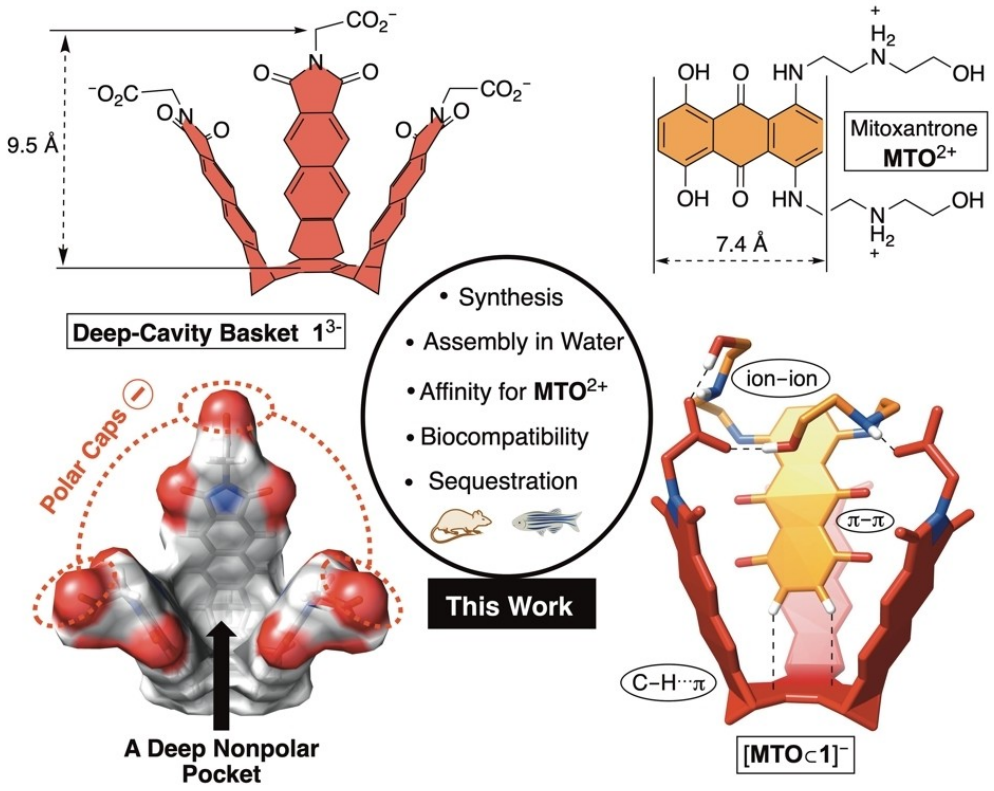

Figure 1. Chemical structures of deep-cavity $\mathbf{1}^{3-}$ and mitoxantrone $\mathbf{MTO}^{2+}$. Top view of energy minimized $\mathbf{1}^{3-}$ (OPLS3e) along with side-view of $[\mathbf{MTO}\subset\mathbf{1}]^{-}$ in which mitoxantrone $\mathbf{MTO}^{2+}$ occupies the binding pocket of $\mathbf{1}^{3-}$.

animals? Can $\mathbf{1}^{3-}$ rescue cells from exposure to lethal quantities of mitoxantrone? With the objective of examining the potential of $\mathbf{1}^{3-}$ as a novel sequestering agent,[21] we studied its (a) synthesis, (b) assembly characteristics, (c) in vitro (different cell lines) and in vivo (zebra fish and rats) biocompatibility, and (d) capacity for trapping and modulating the activity of $\mathbf{MTO}^{2+}$ in both abiotic and biotic systems.

Results and Discussion

Synthesis, Characterization, and Assembly of Deep-Cavity $\mathbf{1}^{3-}$ in Water

To extend and functionalize the sides of *tris*-naphthalene basket[14] (*t*-NB, Figure 2A) we hydrolyzed its methyl esters. The hexaacid product was treated with Ac_2O to give *tris*-anhydride, which was then subjected to condensation with glycine thereby forming deep-cavity **1** in 80% yield. Vapor diffusion of hexane into a solution of **1** (CH_2Cl_2:CH_3COCH_3:CH_3OH = 1:1:1) resulted in the formation of single crystals. From X-ray diffraction analysis, cup-shaped **1** (see Figure 4A below) was found to dimerize in solid state by using carboxylates holding onto two encapsulated acetone molecules via –COO–H···O=C(CH_3)$_2$ hydrogen bonds (d = 2.608 Å, Θ = 159.76°).[22] In addition, the concave naphthalimide sides from **1** form C–H···π contacts with methyl groups from acetone (Figure 4A). ^{1}H NMR spectrum of **1** in DMSO-d_6 showed a set of sharp signals corresponding to a C_{3v} symmetric molecule (Figure 2B); for full spectroscopic characterization of **1** in DMSO-d_6, see Figures S1-S4 in Supporting Information. On the contrary, ^{1}H NMR resonances from **1** were broadened when the spectrum was acquired in 30 mM phosphate buffer (PBS) at pH = 7.0 (Figure 2B, 300 K).[23] Heating the sample above room temperature (365 K, Figure 2D) resulted in the appearance of two aromatic peaks. Concurrently, low temperature spectra (i.e., 275 K) revealed the emergence of four aromatic signals, i.e., twice as many as what is expected for a C_{3v} symmetric $\mathbf{1}^{3-}$ (Figure 2D; Figure S12). From earlier studies,[24] we suspected a dimerization of basket taking place in solution. Indeed, the off-diagonal exchange peaks in ^{1}H-^{1}H ROESY at 275 K (Figure 2E; Figures S14–16 but also Figure S17) indicated two sets of exchangeable signals that along with their ^{1}H chemical shifts (i.e. diamagnetic shielding) are in line with the formation of basket-in-basket dimer $[\mathbf{1}_2]^{6-}$ (Figure 2C). That is to say, proton nuclei from baskets $\mathbf{1}_{in}^{3-}$ (green) and $\mathbf{1}_{out}^{3-}$ (blue), within $[\mathbf{1}_2]^{6-}$, undergo a slow chemical exchange. The upfield set of β and γ proton resonances (labeled green in Figures 2C–E) are assigned to $\mathbf{1}_{in}^{3-}$ since it is expected that the protons of the inner basket experience a greater degree of diamagnetic shielding by aromatics from $\mathbf{1}_{out}^{3-}$. Further, when incremental dilution of a 1.0 mM solution of **1** was monitored with calorimetry (ITC, Figure S11), the binding isotherm was found to fit the model describing dimerization. As the formation of stable $[\mathbf{1}_2]^{6-}$ (K_d = 20 μM, 298 K) is driven by enthalpy ($\Delta H°$ = −8.37 kcal/mol; $\Delta S°$ = −6.6 cal/molK), we reason that energy-favorable desolvation of basket's nonpolar pocket ought to be taking place.[16] All the same, after an incremental dilution of 60 μM solution of **1** was monitored with ^{1}H NMR spectroscopy

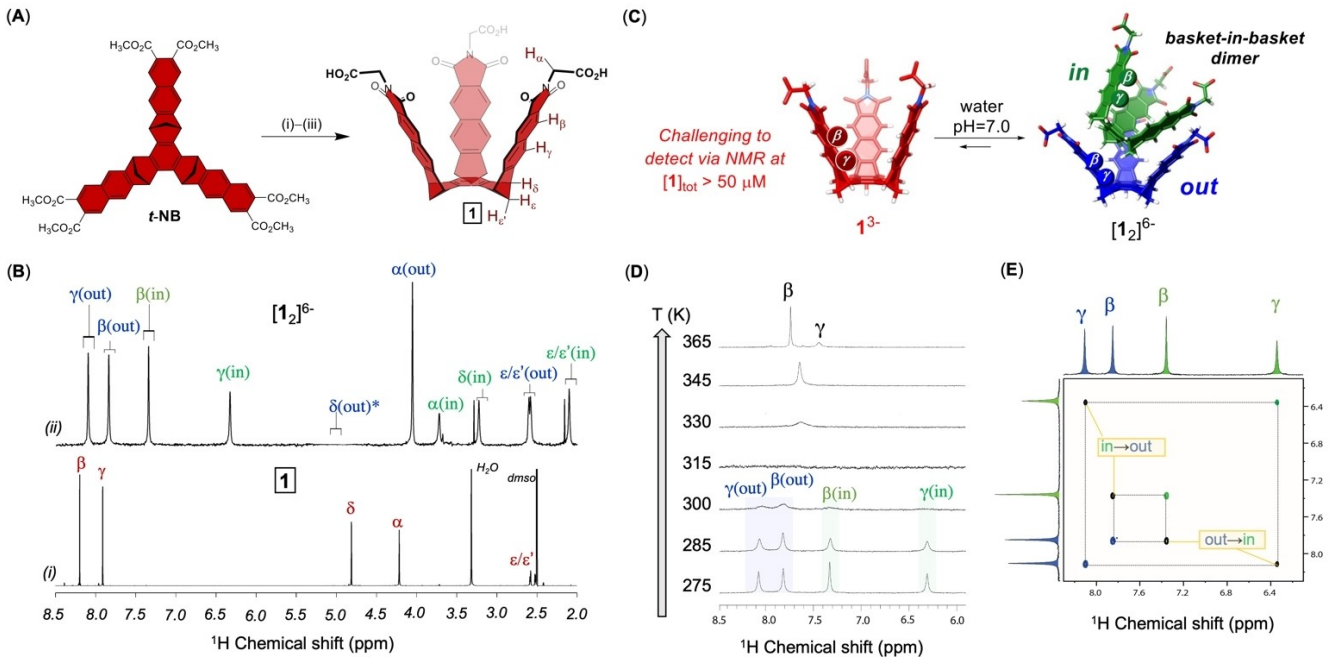

Figure 2. (A) The conversion of ***t*-NB** into **1** proceeds in 81% overall yield; (i) LiOH/THF/Δ, (ii) Ac_2O/Δ, (iii) GlyOH/Cs_2CO_3/AcOH. (B) ^{1}H NMR spectra (850 MHz) of the 150 μM cavitand **1** in (i) DMSO-d_6 at 298 K and (ii) 30 mM PBS (20% D_2O, pH = 7.0) at 275 K.; note that the latter spectrum, corresponding to $[\mathbf{1}_2]^{6-}$, was recorded with water suppression causing the disappearance of $H_{\delta(out)}$ signals. (C) Energy-minimized structures (OPLS3e) of $[\mathbf{1}_2]^{6-}$ and $\mathbf{1}^{3-}$ with their β and γ protons, color coded for three types of magnetic environments (green, blue, and red). (D) Variable temperature ^{1}H NMR spectra (600 MHz, 10% D_2O; water-suppression) of 1.40 mM basket **1** in 30 mM PBS at pH = 7.0. (E) A segment from ^{1}H-^{1}H ROESY NMR spectrum of 0.5 mM of **1** in 30 mM PBS at pH = 7.0 (800 MHz, 275 K, τ_m = 40 ms, 20% D_2O) revealing the exchange of $\mathbf{1}_{in}^{3-}$ (green) and $\mathbf{1}_{out}^{3-}$ (blue) cups from $[\mathbf{1}_2]^{6-}$.

at a lower temperature (275 K, Figure S13) there was a new set of signals emerging under high dilution corresponding to monomeric $\mathbf{1}^{3-}$. As expected, chemical shifts of protons from this species are closer to less magnetically shielded $\mathbf{1}_{out}{}^{3-}$ within $[\mathbf{1}_2]^{6-}$. A Monte-Carlo conformational search (OPLS3e, Schrodinger) of $[\mathbf{1}_2]^{6-}$ revealed several conformers (Figure S49) in which green $\mathbf{1}_{in}{}^{3-}$ occupies the inner space of blue $\mathbf{1}_{out}{}^{3-}$. A representative pose is shown in Figure 2C, with $\mathbf{1}_{in}{}^{3-}$ holding its *tris*-bicyclic bottom against a naphtalimide side arm $\mathbf{1}_{out}{}^{3-}$ while forming C–H···π and π–π intermolecular contacts.

The Mechanism for the Formation of $[\mathbf{1}_2]^{6-}$

As discussed above, slowly exchanging $\mathbf{1}^{3-}$ and $[\mathbf{1}_2]^{6-}$ can both be observed with ^{1}H NMR spectroscopy from highly diluted solutions of **1** at a lower temperature (< 60 μM, Figure S13). Accordingly, studying dynamics of the equilibrium necessitated long NMR acquisitions for obtaining spectra with satisfactory signal-to-noise ratio. With this caveat in mind, we decided to probe the basket's structural and assembly dynamics using the ^{1}H NMR Chemical Exchange Saturation Transfer (^{1}H CEST; Figures S18-20) experiment.[25] CEST is a dynamic NMR method that discloses chemical exchanges in which nuclei from equilibrating molecules (e.g., **A** and **B**) alter chemical/magnetic environment at a slow rate with respect to the chemical shift time scale.[26] The method is particularly valuable for detecting micromolar or lower quantities of exchanging species.[27] Typically, when the pool of interconverting **A** and **B** is highly biased, $p_A \gg p_B$, the signal from minor **B** component is broadened into the baseline. CEST, on the other hand, allows the detection of minor **B** state at ~0.5% threshold. Importantly, the method is just beginning to find its use in the area of supramolecular chemistry[27–28] by providing details about the encapsulation thermodynamics/kinetics of host–guest equilibria[29] in addition to its biochemical application for describing enzyme activity,[30] mapping cell surfaces[31] or determining population distribution of cells.[32] To perform ^{1}H CEST experiments, a radio frequency (RF) pulse (i.e., B_1 field) is swept over the spectral range of interest for which the ^{1}H NMR spectrum is acquired. If the position of such saturating RF pulse is coincident with the chemical shift of minor species **B** then the more easily observable NMR peak of the major state **A** decreases in intensity. The extent to which the signal from **A** is reduced depends on the rate of **A**↔**B** interconversion but also on experimental parameters such as the time the nuclei are allowed to undergo the exchange (T_{ex}) as well as the power of the applied RF pulse. The data is graphed such that the intensity ratio of more populated **A**, with (I) and without (I_0) the saturation pulse (I/I_0) is shown as a function of the chemical shift (i.e., frequency) of the sweeping RF field (Figure S20). This so-called z-spectrum shows "dips" corresponding to the position and population of equilibrating species with information about the rates of their interconversion.[28] Our ^{1}H CEST analysis centered on monitoring well separated signals β and γ from dimer $[\mathbf{1}_2]^{6-}$ dominating in solution: $H_{\beta\text{-}\gamma(out)}$ ($\mathbf{1}_{out}{}^{3-}$, blue in Figure 3A/B) and $H_{\beta\text{-}\gamma(in)}$ ($\mathbf{1}_{in}{}^{3-}$, green in Figure 3A/B). Thus, a series of ^{1}H NMR spectra were acquired with a sweeping RF pulse from 8.5 to 6.0 ppm. The CEST profiles corresponding to $H_{\gamma(out)}$ (part *ii* in Figure 3B) revealed basket $\mathbf{1}_{out}{}^{3-}$ undergoing an exchange with three additional states: $\mathbf{1}_{in}{}^{3-}$ from $[\mathbf{1}_2]^{6-}$ ($H_{\gamma(in)}$ at 6.4 ppm, visible in ^{1}H NMR), $\mathbf{1}_{(R)}{}^{3-}$ ($H_{\gamma(R)}$ at 7.7 ppm, invisible in ^{1}H NMR) and $\mathbf{1}_{(S)}{}^{3-}$ ($H_{\gamma(S)}$ at 6.5 ppm, invisible in ^{1}H NMR). With four states interconverting slow on the NMR time scale, we proceeded to fit I/I_0 intensities vs. B_1 field positions by using Bloch-McConnell equations describing different four-state exchange scenarios. The best fit, obtained from grid search of a χ^2 surface (Figures S21-25 and Table S2), corresponds to mechanism in which dimer $[\mathbf{1}_2]^{6-}$ turns into monomer $\mathbf{1}_{(R)}{}^{3-}$ followed by its conversion into $\mathbf{1}_{(S)}{}^{3-}$ (Figure 3A). Since chemical shift of "invisible" γ aromatic protons from $\mathbf{1}_{(S)}{}^{3-}$ became available through ^{1}H CEST, the simultaneous lineshape analysis of ^{1}H NMR spectra obtained by incremental dilution of a solution of **1** (Figure 3C) along with ^{1}H CEST data (Figure S26 and Table S3) was attempted. From a satisfactory fit, the analysis not only supported the interconversion mechanism (i.e., $[\mathbf{1}_2]^{6-} \rightleftharpoons 2[\mathbf{1}_{(R)}]^{3-} \rightleftharpoons 2[\mathbf{1}_{(S)}]^{3-}$ in Figure 3A) but also provided kinetic and thermodynamic parameters to describe it. The stability of $[\mathbf{1}_2]^{6-}$ with respect to the dominant monomeric state $\mathbf{1}_{(R)}{}^{3-}$ was thus found to be $K_d(1) = 3.2$ μM while $K_{eq} = [\mathbf{1}_{(S)}{}^{3-}]/[\mathbf{1}_{(R)}{}^{3-}] = 0.15$ (Figure 3A).

On the Nature of Monomeric $\mathbf{1}_{(R)}{}^{3-}$ and $\mathbf{1}_{(S)}{}^{3-}$

What is the difference between monomers $\mathbf{1}_{(S)}{}^{3-}$ and $\mathbf{1}_{(R)}{}^{3-}$? To address this question, we subjected energy-minimized $\mathbf{1}^{3-}$ to hybrid replica exchange molecular dynamics (hybrid REMD) simulation.[33] REMD is a method[34] in which parallel molecular dynamics (MD) simulations are run at different temperatures with conformational states being moved from one temperature bath to another for more effective sampling of the conformational space and overcoming high-energy barriers for interconversion.[35] While standard REMD uses all solvent molecules to calculate exchange energies for replicas, hybrid REMD employs a specified number of solvent molecules making it more suitable for examining the conformational dynamics of explicitly solvated systems. After running a hybrid REMD simulation of $\mathbf{1}^{3-}$, we noted that averaged distance between carboxylates at top of the cavitand showed a bimodal distribution centered at circa 5 and 8 Å (Figure S52). With predominant conformers of $\mathbf{1}^{3-}$ having a greater distance between carboxylates we decided to refer to this ensemble of states as relaxed ($\mathbf{1}_{(R)}{}^{3-}$). On the other side, less populated conformational states having carboxylates (i.e., naphthalimide sides) at a closer distance are labeled as squeezed ($\mathbf{1}_{(S)}{}^{3-}$, Figure 4B). As discussed earlier, CEST measurements in Figure 3B are in line with two monomeric states of $\mathbf{1}^{3-}$ having $H_{\beta/\gamma}$ protons less (minor state) or more (major state) shielded. We reason that these experimentally distinguishable conformers are congruent with the computed $\mathbf{1}_{(S)}{}^{3-}$ and $\mathbf{1}_{(R)}{}^{3-}$. That is to say, the separation of naphthylimide arms within $\mathbf{1}^{3-}$ is expected to have effect on diamagnetic anisotropy that these aromatics impose on one another therefore making $H_{\beta/\gamma}$ protons more (for

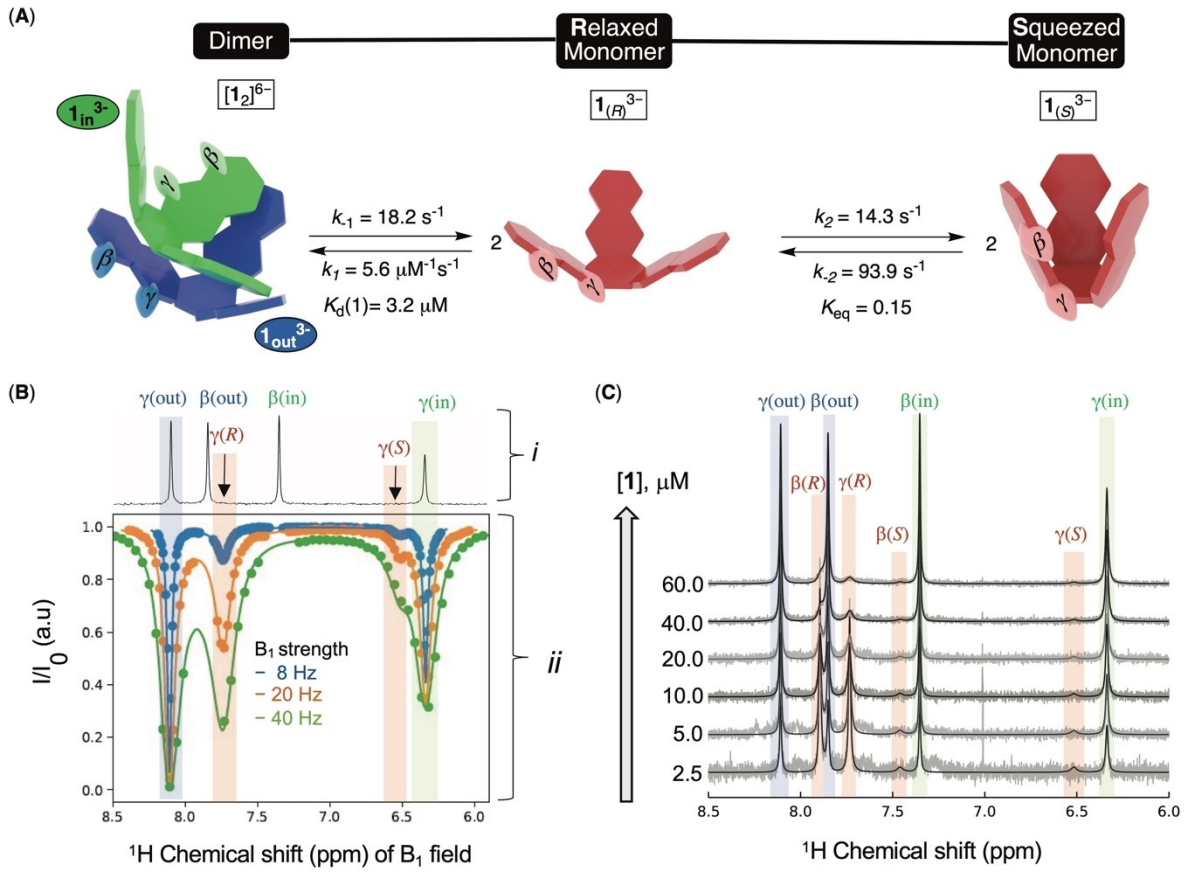

Figure 3. (A) A graphical representation of the mechanism by which basket **1** assembles in water with thermodynamic (K_d and K_{eq}) and kinetic (k, rate coefficients) parameters obtained by global lineshape analysis described in C below. (B) (i) A region of ^{1}H NMR spectrum (850 MHz, 275 K) of 150 μM solution of **1** in 30 mM PBS at pH = 7.0 (20% D_2O) showing four aromatic peaks corresponding to $[\mathbf{1}_2]^{6-}$. (ii) z-spectra of $H_{\gamma(out)}$ (blue shade) were obtained with sweeping 8, 20, and 40 Hz B_1 fields. The experimental data (dots) were fit to the model shown in panel A (solid lines) to give thermodynamic and kinetic parameters pertaining the equilibria. (C) The aromatic region of experimental ^{1}H NMR spectra (850 MHz, 275 K) of 2.5 to 60 μM of **1** in 30 mM PBS at pH = 7.0 (20% D_2O) overlayed with simulated spectra (black) obtained from simultaneous analysis of ^{1}H lineshapes and CEST experiments. Plotted intensities have been normalized by the total concentration of **1**.

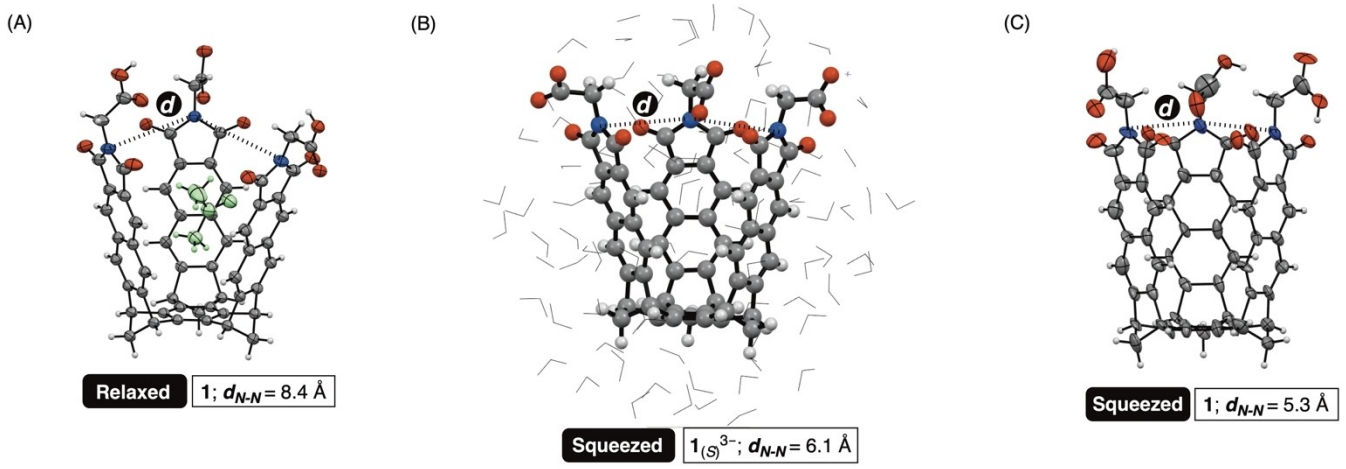

Figure 4. (A) An ORTEP representation (50% probability) of X-ray structure of basket **1** with a molecule of acetone occupying its inner space. Single crystals of **1** were obtained by vapor diffusion of hexane into its CH_2Cl_2:CH_3COCH_3:CH_3OH = 1:1:1 solution. (B) A representative structure of squeezed $\mathbf{1}_{(S)}^{3-}$ obtained from hybrid REMD simulation of basket in a box of water molecules; note that wireframe representation to show (some H_2O molecules. (C) An ORTEP representation of squeezed **1** obtained from MicroED measurement of its solid precipitated from an aqueous solution of $\mathbf{1}^{3-}$ by acidification.

$\mathbf{1}_{(S)}^{3-}$) or less (for $\mathbf{1}_{(R)}^{3-}$) shielded. Importantly, a collapse of naphthylimides in $\mathbf{1}_{(S)}^{3-}$ leads to expulsion of water molecules (Figure S54–55) to give a "squeezed" and strained conformer (Figure 4B). Perhaps, such dehydration of naphthalimide arms[36]

driven by the hydrophobic effect, off-sets the energetic cost of strain developed by bringing them together.[37] Additionally, adding HCl_{aq} to a solution of **1** in water resulted in protonation and precipitation of the basket. The solid obtained upon lyophilization was subjected to microcrystal electron diffraction (MicroED) analysis,[38] which revealed "squeezed" and unoccupied cavitands assembling in the solid state (Figure 4C). Additionally, the average distance between naphthalimide sides ($d_{N\text{-}N}$ in Figure 4C) is 5.3 Å and thus close to 6.1 Å for computed $\mathbf{1}_{(S)}^{3-}$ (Figure 4B). As discussed earlier, the crystallization of **1** from organic solvents resulted in the formation of acetone populated **1** (Figure 4A) that resembles $\mathbf{1}_{(R)}^{3-}$ with $d_{N\text{-}N}$ = 8.4 Å.

Inclusion Complexation of Mitoxantrone (MTO^{2+}) in Abiotic Systems

An incremental addition of a standard solution of $\mathbf{MTO}^{2+}$ to **1** in PBS at pH = 7.0 caused the emergence of a set of ^{1}H NMR signals (pink in Figure 5A) from the bound host in addition to a group of magnetically shielded resonances from bound $\mathbf{MTO}^{2+}$ (H_A in Figure 5A). First, adding more than one molar equivalent of the $\mathbf{MTO}^{2+}$ led to broadening and loss of ^{1}H NMR signals with the concomitant appearance of a precipitate (Figures S27; see also Figures S29-30). In a separate experiment, the precipitate obtained from mixing host and guest at **1** : **MTO** = 1 : 6 was isolated via centrifugation. Measuring ^{1}H NMR spectrum of such precipitate (DMSO-d_6, Figure S27B) we found that host-guest stoichiometry corresponds to zwitterionic $\mathbf{1}_2\mathbf{MTO}_3$; with no structural data about $\mathbf{1}_2\mathbf{MTO}_3$, we refrain from commenting about the mode of binding. Second, at approximately equal proportion of **1** and $\mathbf{MTO}^{2+}$ in solution signals from the free host were fully displaced by those from the bound species indicating the formation of binary and stable $[\mathbf{MTO}\subset\mathbf{1}]^-$ occurring slow on the chemical shift time scale. In support of this, DOSY NMR measurements (Figures S40-43) showed the complexed basket diffusing at the same rate at as $\mathbf{MTO}^{2+}$ with r_H = 12.2 Å and in an agreement with the computed radius of $[\mathbf{MTO}\subset\mathbf{1}]^-$ (Figure 5B). Finally, time-of-flight mass spectrometry measurement of a drug-basket mixture revealed the formation of binary $[\mathbf{MTO}\subset\mathbf{1}]^-$ (Figure S28). The splitting of ^{1}H NMR resonances from $[\mathbf{MTO}\subset\mathbf{1}]^-$ indicates C_s symmetry of the complex (Figure 5A). That is to say, signals from $\mathbf{1}^{3-}$ were within $[\mathbf{MTO}\subset\mathbf{1}]^-$ divided into three chemically distinct groups (e.g.,

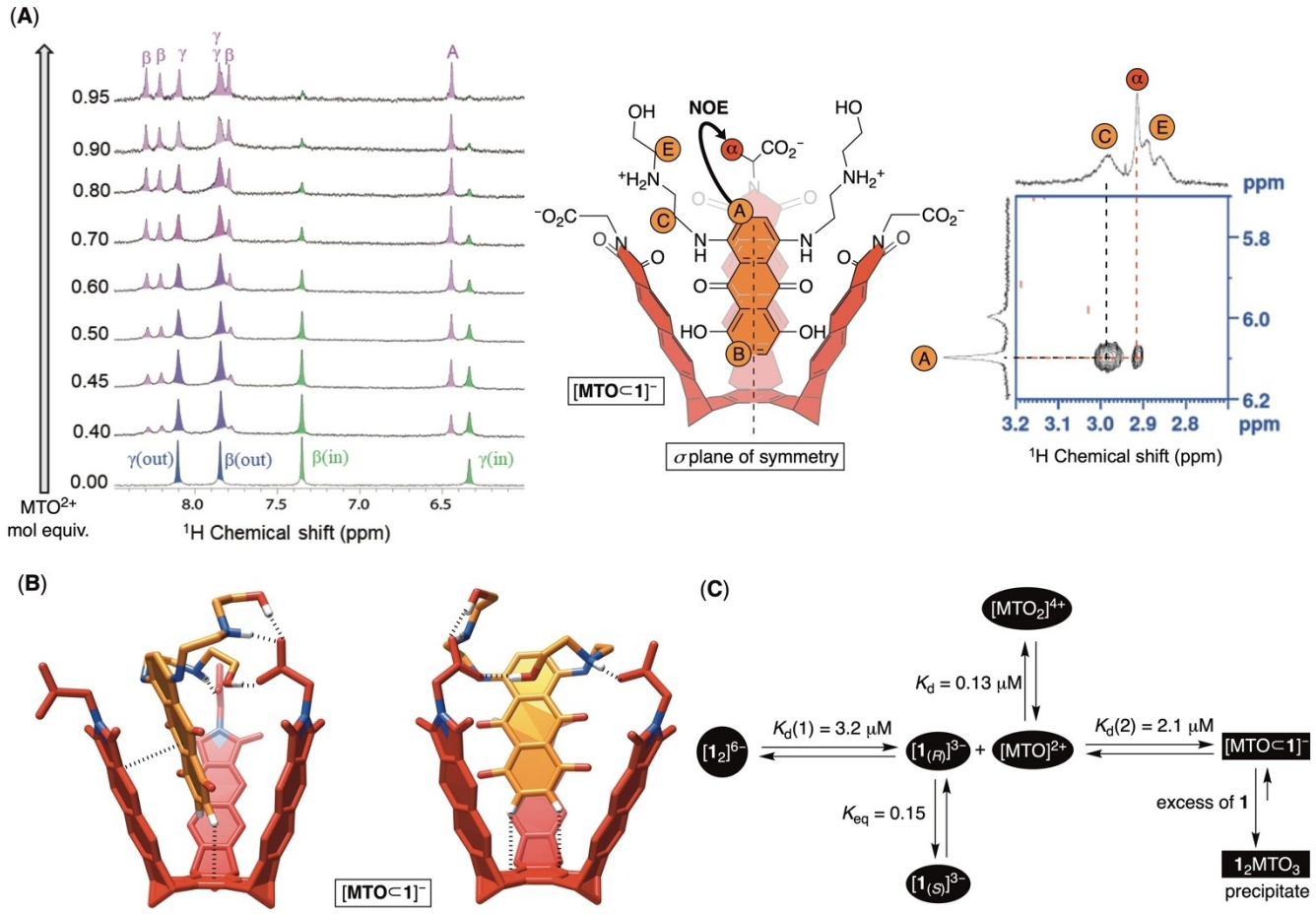

Figure 5. (A) A segment from ^{1}H NMR spectra (850 MHz, 275 K) obtained upon an incremental addition of 500 μM standard solution of $\mathbf{MTO}^{2+}$ to 150 μM solution of **1** in 30 mM PBS at pH = 7.0 (20% D_2O). A chemical representation of C_s symmetric $[\mathbf{MTO}\subset\mathbf{1}]^-$ with color coded proton nuclei. (Right) Partial ^{1}H-^{1}H NOESY spectrum (850 MHz, 275 K) of 70 μM $[\mathbf{MTO}\subset\mathbf{1}]^-$ in 30 mM PBS at pH = 7.0 (20% D_2O) showing the correlation (red) of H_α form the $\mathbf{1}^{3-}$ and H_A from $\mathbf{MTO}^{2+}$. (C) Side views of a representative and energy-minimized structure (OPLS3e) of $[\mathbf{MTO}\subset\mathbf{1}]^-$. (C) Thermodynamic parameters for equilibria of basket **1** and $\mathbf{MTO}^{2+}$ were determined in 30 mM PBS at pH = 7.0 and 275 K.

three H_β and H_γ in Figure 5A) having the relative integration commensurate with the molecule possessing a single plane of symmetry. For a full assignment of all resonances corresponding to [**MTO**⊂**1**]$^-$, we completed ^{1}H/^{1}H COSY, TOCSY, HSQC and NOESY measurements (Figures S33–S39 and Table S4). A great magnetic shielding of aromatic H_β protons from **MTO**$^{2+}$ ($\Delta\delta =$ 2.42 ppm, Figure 5A) is consistent with these nuclei residing deep inside the aromatic pocket of **1**$^{3-}$. Concurrently, H_A protons from the drug experienced a smaller chemical shift perturbation ($\Delta\delta = 0.72$ ppm) but also NOE cross correlation with H_α at the rim of **1**$^{3-}$ (Figure 5A). It follows that H_A nuclei occupy the space at the host's rim where the magnetic shielding is reduced. Inserting the anthraquinone ring from **MTO**$^{2+}$ into the pocket of **1**$^{3-}$ to π–π stack with one of its naphthalimides gives C_s symmetric [**MTO**⊂**1**]$^-$ (Figure 5A). Indeed, the results of Monte Carlo conformational search (Figure 5B; Figure S50) confirmed this mode of binding in which the ammonium and hydroxyl groups from **MTO**$^{2+}$ complement the host's carboxylates by forming hydrogen bonds. To quantify the thermodynamic stability of [**MTO**⊂**1**]$^-$, we turned to ^{1}H NMR spectroscopic titration at 275 K wherein most of the species interconvert at a slow rate slow on the NMR time scale. That is to say, basket **1** at a sufficiently low concentration and in the presence of less than equimolar amount of **MTO** was expected to partition into $\mathbf{1}_{(R)}^{3-}$, $\mathbf{1}_{(S)}^{3-}$, $[\mathbf{1}_2]^{6-}$ and [**MTO**⊂**1**]$^-$ with ^{1}H NMR signals corresponding to each of these species being well resolved. Concurrently, **MTO** also distributes between its monomeric **MTO**$^{2+}$ and dimeric $[\mathbf{MTO}_2]^{4+}$ forms.[39] First, we prepared a solution of 4.0 μM basket **1** containing 2.0 μM mitoxantrone with the excess of the host preventing the formation of higher order aggregates and precipitation. Next, ^{1}H NMR spectrum of the mixture (Figure S31) revealed signals corresponding to $\mathbf{1}_{(R)}^{3-}$, $[\mathbf{1}_2]^{6-}$ and [**MTO**⊂**1**]$^-$ with their integration permitting accurate determination (via deconvolution analysis; Figure S32) of their corresponding concentrations including $\mathbf{1}_{(S)}^{3-}$. Importantly, the signals of free monomeric **MTO**$^{2+}$ and dimeric $(\mathbf{MTO}_2)^{4+}$ were broadened into the baseline. To determine the concentration of uncomplexed drug, we simply subtracted the portion of the drug included in [**MTO**⊂**1**]$^-$ from its total concentration. This amount of **MTO** is distributed between its monomeric and dimeric form, which can be determined from $K_d = 0.13$ μM.[39] From known concentrations of all equilibrating species in Figure 5C, we obtained the corresponding equilibrium constants: the stability of $[\mathbf{1}_2]^{6-}$ is $K_d(1) = 3.5$ μM while the affinity of monomeric $\mathbf{1}_{(R)}^{3-}$ toward **MTO**$^{2+}$ is $K_d(2) = 2.1$ μM.

Sequestration of Mitoxantrone (MTO^{2+}) with Basket 1^{3-} in Abiotic Systems using Light/pH as Stimuli

A steady UV irradiation of a solution of **1** (i.e., predominantly $[\mathbf{1}_2]^{6-}$) resulted in decarboxylation[40] of the basket followed by precipitation of insoluble product **2** (Figure 6; see also Figure S46); ^{1}H NMR spectrum of the precipitate in DMSO revealed the sole formation of this compound. When we irradiated 0.32 mM solution of **1** and 0.20 mM **MTO**$^{2+}$, the effective

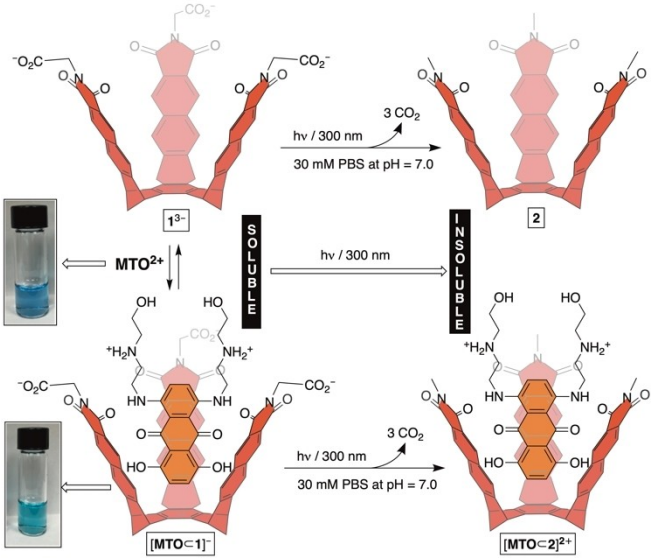

Figure 6. (Top) A photodecarboxylation of **1**$^{3-}$ gives **2** that is insoluble in water (Figures S7-9). (Bottom) When the same photochemical transformation is repeated in the presence of **MTO**, the drug precipitates along with **2** in the form of [**MTO**⊂**2**]$^{2+}$ (Figure S46). (Snapshots on far-left side) A 70 μM solution of **MTO** in 30 mM PBS at pH = 7.0) is blue. Upon the addition of basket **1** (140 μM), the solution turns turquois.

removal of the drug took place by precipitation (99.5% by fluorescence, Figures S46-47). In contrast, an irradiation of a solution of **MTO** did not cause any precipitation, with drug molecules remaining intact (Figure S44). Based on prior studies,[40a,41] we reason that our cavitand must have formed an inclusion complex with **MTO**$^{2+}$ so that after decarboxylation the drug was rendered insoluble in the form of a host–guest complex (Figure 6). Indeed, adding a colorless solution of **1** to a blue solution of **MTO**$^{2+}$ resulted in color changing to turquois to indicate the formation of a noncovalent host-guest complex (Figure 6).[42] In the similar manner, lowering the pH of 50 μM solution of **MTO** and **1** (300 μM) from 7.0 to 2.0 resulted in the formation of blue precipitate with fluorescence measurements (Figure S48) confirming the removal of the drug from solution (74% precipitated). This time, protonation of basket's carboxylates would reduce the solubility at the lower pH to trigger precipitation of basket-drug complexes. The process is reversible, and the precipitate can be redissolved by raising pH from 2.0 to 7.0.

Biocompatibility and Bioactivity of Deep-Cavity 1^{3-}

Human umbilical vascular endothelial cells (HUVECs) were grown in a medium containing 100 μM of deep-cavity **1** for two days. On the basis of immunocytochemistry imaging (Figure 7A), cells' vascular morphology and viability remained unaltered. Moreover, baskets had no effect on the proliferation of HUVECs (MTS) with the absence of cytotoxicity (LDH) being in line with the innocuous nature of our abiotic host. Interestingly, a mild neurotoxic effect (~15% of cell death, Figure 7B) was measured on highly sensitive human neurons

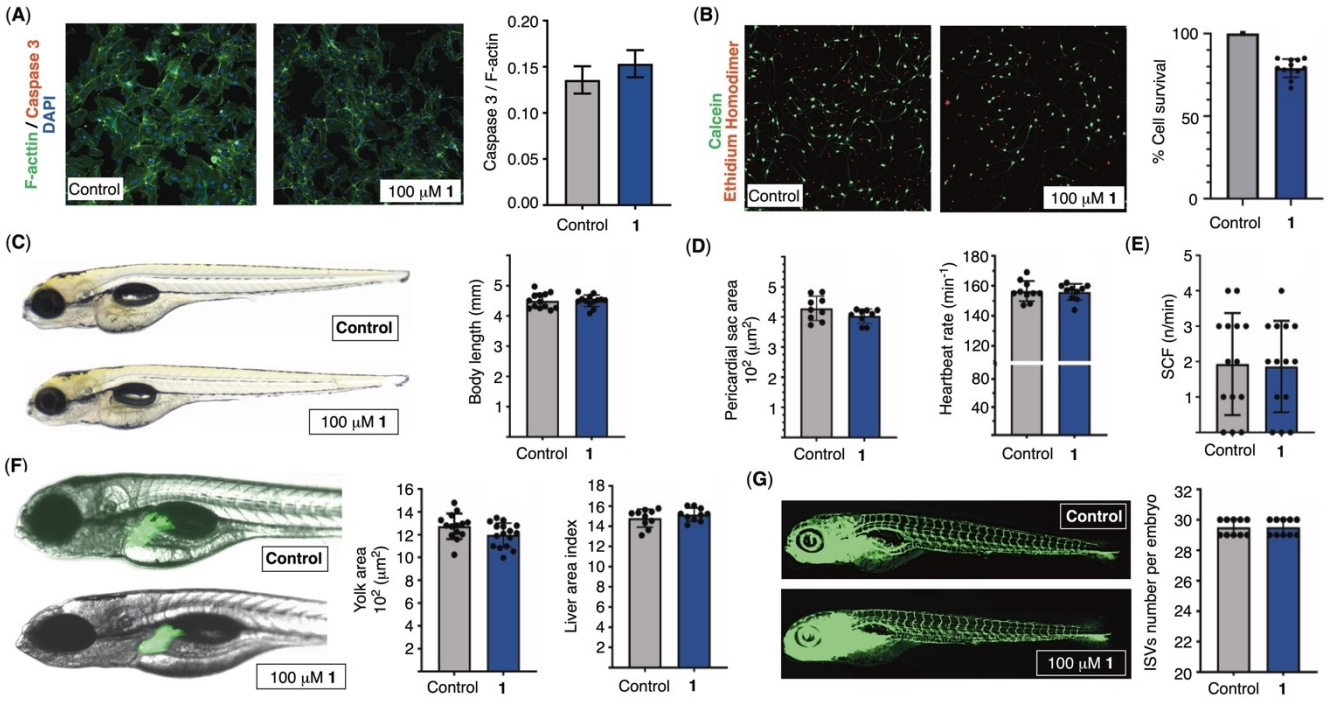

Figure 7. (A) Immunocytochemistry images of HUVECs treated with PBS (control) and 100 μM solution of **1** were obtained 48 h post-treatment using staining for F-actin, DAPI, and caspase 3. (B) Images of human iPSCs treated with PBS (control) and 100 μM solution of **1** were obtained 72 h post-treatment using calcein and ethidium homodimer. (C/D) AB zebrafish embryos at six hours post-fertilization (hpf) stage were treated with PBS (control) or 100 μM of **1**. After five days, the embryos were imaged and measured for body length (C) as well as for pericardial sac area and heart beating rate (D) at 120 hpf. (E) At 6 hpf stage, AB zebrafish embryos were treated with (control) or 100 μM of **1**. Spontaneous contraction frequency (SCF) was inspected at 30 hpf for a period of one minute. (F) Transgenic *Tg*(*-2.8fabp10a*:EGFP) zebrafish embryos with fluorescently labelled liver (green) were treated at 72 hpf stage with 0.1% PBS (control) or 100 μM of **1** and imaged using fluorescence microscopy at 120 hpf. The yolk sac and liver area index were then determined. (G) Transgenic *Tg*(*fli1*:EGFP) zebrafish embryos with fluorescently labelled endothelial cells (green) treated at 6 hpf stage with 0.1% PBS (control) or 100 μM of **1** and imaged using fluorescence microscopy at 120 hpf. The number of intersegmental vessels (ISVs) were then determined.

cultured over three days under comparable experimental conditions. Motivated by in vitro findings, we turned to examine the toxicity of deep-cavity **1** toward zebrafish embryos (Figure 7C–G).[43] While the study group was exposed to 100 μM of **1**, the control group of embryos resided in embryo water (10% PBS) over the course of five days. First, there was no death detected in each group of fish. Second, deep-cavity **1** showed no harmful effects on zebrafish embryo body length (Figure 7C), cardiovascular system (Figure 7D), nervous system function (Figure 7E), liver development and function (Figure 7F) or vasculature (Figure 7G).[44] To examine the cavitand's toxicity on mammals, we turned to working with Wistar albino rats (Figure 8).[45] Thus, a single dose of **1** was, orally (**O**) and intraperitoneally (**IP**), administered into rats. Over the course of fourteen days, we detected no statistically significant changes of the body weight with respect to control (Figure 8A). Moreover, there was no difference in food and water intake (Figure 8A) as well as normalized organ weight (Figure 8C). To probe the cardiotoxicity of deep-cavity **1**, we perfused 26.0 μM solution of the basket through an isolated rat heart for five minutes (the Langendorff technique; Figure 8D).[46] There were no changes in cardio dynamic parameters and coronary flow. Histological analyses of heart, liver, kidney, and brain tissues isolated from **O** and **IP** treated rats showed no signs of abnormal and modified morphology (Figure S57). The genotoxicity of deep-cavity **1** was evaluated using hepatocytes isolated from the liver of **O** and **IP** treated rats via alkaline comet assay (Figure 8B; Table S10). Importantly, no statistically significant differences were found in total comet scores relative to the negative control, which with predominant formation of T_0 and T_1 comets suggests no DNA damage.

To probe the effect of **1** on the action of anticancer **MTO**$^{2+}$, we used LDH assay to monitor the activity (i.e., cell death) of epithelial breast cancer cells (MDA-MD-231) in a medium containing these compounds at two arbitrarily chosen but seemingly limiting ratios (Figure 8E). As expected, the cytotoxicity of **MTO**$^{2+}$ was, after 48 h, found to be 50% (Figure 8E). On the contrary, deep-cavity **1** would under the same conditions act as a nearly nontoxic compound (8%, Figure 8E). When **1** and **MTO**$^{2+}$ were used simultaneously and at the molar ratio of 2:1, the cytotoxicity increased to 62%. The result suggests that baskets assisted the transport of drug molecules into cancer cells to boost their anticancer activity – a hypothesis that warrants further investigation. In contrast, a greater proportion of the cavitand (i.e., **1**:**MTO**$^{2+}$ = 4:1; Figure 8E) resulted in MTOs cytotoxicity dropping to 36%. While 1:2 and 1:4 ratios of drug-to-host appear limiting, a systematic study is expected to provide a more clear understanding of the observation. For now, we hypothesize that at higher basket-to-drug proportions,

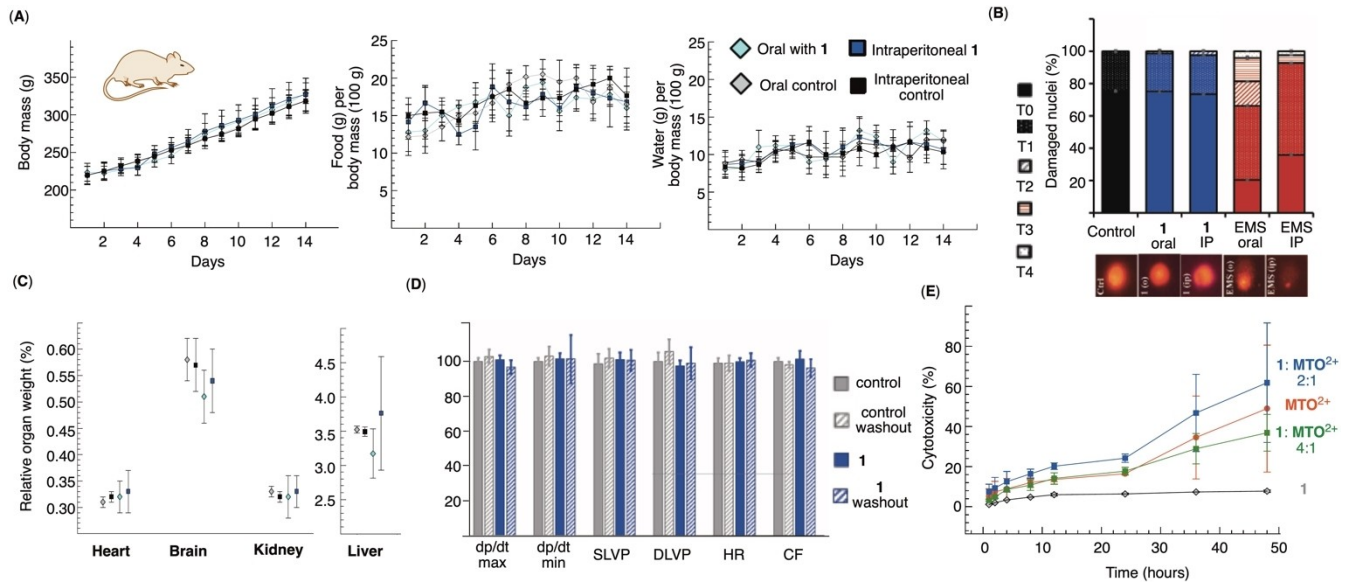

Figure 8. Wistar albino rats were administered a single dose of PBS or basket **1**, orally (2.0 ml; 2.6 mM of **1**) or intraperitoneally (1.0 ml; 2.6 mM of **1**). After 14 days, we recorded body mass, food, and water intake per body mass (A) as well as organ weight normalized by total body weight (C). (B) Hepatocytes isolated from rats, sacrificed 24 h after receiving a single oral or intraperitoneal dose, were assessed via the alkaline comet assay. Negative controls were untreated animals, while positive controls were rats treated with 300 mg/kg of EMS alkylating agent. (D) An isolated heart from treated Wistar albino rats was perfused by PBS (control) or 26 μM solution of **1** for five minutes. Cardio dynamic parameters are reported as: maximum and minimum rate of pressure (dp/dt), systolic and diastolic left ventricular pressure (SLVP and DLVP), heart rate (HR), and coronary flow (CF). (E) Lactate dehydrogenase (LDH) essay was used to quantify cytotoxicity of 10 μM **MTO**$^{2+}$ and 20 μM **1** or both in different proportions on epithelial breast cancer line of cells (MDA-MD-231). The cells were seeded into a well plate for 24 h in media. The media was then exchanged with fresh media supplemented with solutions of **1**, basket + **MTO**$^{2+}$ or **MTO**$^{2+}$ in 30 mM PBS at pH = 7.0 at the represented concentrations. Each experiment was conducted twice, with the results showed as mean ± standard deviation.

baskets must be holding onto mitoxantrone more effectively to, perhaps, prevent its intercalation into DNA topoisomerases.

Conclusions

Deep-cavity $\mathbf{1}^{3-}$ is a novel, biocompatible, and modular host with distinct conformational and assembly characteristics. In water, the cavitand exists as dimer $[\mathbf{1}_2]^{6-}$ in equilibrium with two $\mathbf{1}^{3-}$ monomeric states. The more stable $\mathbf{1}_{(R)}{}^{3-}$ has water-solvated inner space ready to accommodate a guest, while the less stable $\mathbf{1}_{(S)}{}^{3-}$ has its inner space desolvated with aromatic walls collapsing on the space. Using a combination of ^{1}H NMR CEST, hybrid REMD, MicroED and VT ^{1}H NMR data, we further quantified kinetics and thermodynamics of these equilibria thereby demonstrating the utility of such computational and experimental methods outside a supramolecular chemist's standard toolbox. Importantly, deep-cavity $\mathbf{1}_{(R)}{}^{3-}$ includes cytotoxic mitoxantrone (**MTO**$^{2+}$) into its pocket to give binary $[\mathbf{MTO}\subset\mathbf{1}]^-$ ($K_d = 2.1$ μM). In consequence, **MTO**$^{2+}$ can be easily removed from its micromolar aqueous solutions containing deep-cavity $\mathbf{1}^{3-}$ by light irradiation or lowering the solution's pH. With regard to biocompatibility, both in vitro and in vivo measurements are in line with the innocuous nature of **1**. On top of that, at higher proportions of **1** with regard to **MTO**$^{2+}$, the active concentration of the drug seems to be reduced to restore the cells' normal function. As novel, accessible, and biocompatible hosts, we reason that deep-cavity baskets hold promise for developing supramolecular antidotes capable of sequestering a broad range of aromatic toxicants in complex biological systems.

Experimental Section

Experimental details about standard computational work and experimental measurements are provided in Supporting Information.

Acknowledgements

This work was supported with funds from the NIH (NIDA) under NIH-R21DA052444 and NSF under CHE-2002781. This work was also supported by The Foundation for a Better World. The authors are grateful to the Ministry of Science, Technological Development, and Innovations of the Republic of Serbia for support (451-03-47/2023-01-200042, 200111 and 200378). We thank NSF Graduate Research Fellowships Program (GRFP) for support to graduate student A.M. Electron microscopy was performed at the Center for Electron Microscopy and Analysis (CEMAS) while NMR at CCIC NMR facility at The Ohio State University. Generous computational resources from the OSC are gratefully acknowledged.

Conflict of Interests

The authors declare no conflict of interest.

Data Availability Statement

The data that support the findings of this study are available from the corresponding author upon reasonable request.

Keywords: anticancer agents · cavitands · mitoxantrone · sequesters · supramolecular chemistry

[1] a) G. T. Edward, E. Orton, R. Baker, D. Kendrick, K. Sayal, *J Public Health* **2017**, *39*, e1-e9; b) J. M. Bertolote, A. Fleischmann, M. Eddleston, D. Gunnell, *Br. J. Psychiatry* **2006**, *189*, 201–203; c) H. J. De Silva, N. A. Samarawickrema, A. R. Wickremasinghe, *Trans. R. Soc. Trop. Med. Hyg.* **2006**, *100*, 803–806; d) from *National Institute of Drug Abuse*, see https://nida.nih.gov/drug-topics/trends-statistics/overdose-death-rates.

[2] a) L. Zhang, J. C. Leroux, *Adv. Drug Delivery Rev.* **2015**, *90*, 1–2; b) Y.-C. Pan, Y.-X. Yue, X.-Y. Hu, H.-B. Li, D.-S. Guo, *Adv. Mater.* **2021**, *33*, 2104310; c) V. Forster, J. C. Leroux, *Sci. Transl. Med.* **2015**, *7*, 290–298; d) J. C. Leroux, *Nat. Nanotechnol.* **2007**, *2*, 679–684.

[3] B. Chacko, J. V. Peter, *Indian J. Crit. Care Med.* **2019**, *23*, S241-S249.

[4] a) C. L. Deng, S. L. Murkli, L. D. Isaacs, *Chem. Soc. Rev.* **2020**, *49*, 7516–7532; b) H. Yin, D. Bardelang, R. Wang, *Trends Chem.* **2021**, *3*, 1–4.

[5] a) C.-H. Chen, T.-H. Huang, A. O. Elzoghby, P.-W. Wang, C.-W. Chang, J.-Y. Fang, *Int. J. Nanomed.* **2017**, *12*, 8071–8083; b) Y. Chen, Y. Zhang, J. Zhuang, J. H. Lee, L. Wang, R. H. Fang, W. Gao, L. Zhang, *ACS Nano* **2019**, *13*, 7209–7215.

[6] F. Xu, T. Kang, J. Deng, J. Liu, X. Chen, Y. Wang, L. Ouyang, T. Du, H. Tang, X. Xu, S. Chen, Y. Du, Y. Shi, Z. Qian, Y. Wei, H. Deng, M. Gou, *Small* **2016**, *12*, 2067–2076.

[7] E. F. Duran-Lara, J. L. Marple, J. A. Giesen, Y. Fang, J. H. Jordan, W. T. Godbey, A. Marican, L. S. Santos, S. M. Grayson, *Biomacromolecules* **2015**, *16*, 3434–3444.

[8] S. Rojas, T. Baati, L. Njim, L. Manchego, F. Neffati, N. Abdeljelil, S. Saguem, C. Serre, M. F. Najjar, A. Zakhama, P. Horcajada, *J. Am. Chem. Soc.* **2018**, *140*, 9581–9586.

[9] L. C. Smith, P. T. Bremer, C. S. Hwang, B. Zhou, B. Ellis, M. S. Hixon, K. D. Janda, *J. Am. Chem. Soc.* **2019**, *141*, 10489–10503.

[10] C. Xu, X. Yang, X. Fu, R. Tian, O. Jacobson, Z. Wang, N. Lu, Y. Liu, W. Fan, F. Zhang, G. Niu, S. Hu, I. U. Ali, X. Chen, *Adv. Mater.* **2017**, *29*, 1603673.

[11] a) T. J. Finnegan, V. W. L. Gunawardana, J. D. Badjic, *Chem. Eur. J.* **2021**, *27*, 13280–13305; b) S. Zhou, W. Li, Q. Zhao, H. Dong, Y. Wang, F. Lu, J. Zhao, S. Liu, H. Chen, L. Wang, W. Liu, M. Zhang, S. Chen, *ACS Appl. Mater. Interfaces* **2021**, *13*, 58291–58300; c) W. Xue, P. Y. Zavalij, L. Isaacs, *Angew. Chem. Int. Ed.* **2020**, *59*, 13664; d) U. Hoffmann, M. Grosse-Sundrup, K. Eikermann-Haerter, S. Zaremba, C. Ayata, B. Zhang, D. Ma, L. Isaacs, M. Eikermann, *Anesthesiology* **2013**, *119*, 317–325.

[12] A. K. Pannu, *Curr. Drug Metab.* **2019**, *20*, 714–719.

[13] A. Bom, M. Bradley, K. Cameron, J. K. Clark, J. Van Egmond, H. Feilden, E. J. MacLean, A. W. Muir, R. Palin, D. C. Rees, M.-Q. Zhang, *Angew. Chem. Int. Ed.* **2002**, *41*, 265–270.

[14] Z. Lei, M. J. Gunther, V. W. Liyana Gunawardana, R. Z. Pavlovic, H. Xie, X. Zhu, M. Keenan, A. Riggs, J. D. Badjic, *Chem. Commun.* **2020**, *56*, 10243–10246.

[15] R. Z. Pavlovic, R. F. Lalisse, A. L. Hansen, C. A. Waudby, Z. Lei, M. Gueney, X. Wang, C. M. Hadad, J. D. Badjic, *Angew. Chem. Int. Ed.* **2021**, *60*, 19942–19948.

[16] F. Biedermann, W. M. Nau, H.-J. Schneider, *Angew. Chem. Int. Ed.* **2014**, *53*, 11158–11171.

[17] J. B. Wittenberg, L. Isaacs, *Supramol. Chem. Mol. Nanomater.* **2012**, *1*, 25–43.

[18] B. J. Evison, B. E. Sleebs, K. G. Watson, D. R. Phillips, S. M. Cutts, *Med. Res. Rev.* **2016**, *36*, 248–299.

[19] S. K. Konda, R. Maliki, S. McGrath, B. S. Parker, T. Robinson, A. Spurling, A. Cheong, P. Lock, P. J. Pigram, D. R. Phillips, L. Wallace, A. I. Day, J. G. Collins, S. M. Cutts, *ACS Med. Chem. Lett.* **2017**, *8*, 538–542.

[20] a) P. Lam, R. D. Lin, N. F. Steinmetz, *J. Mater. Chem. B* **2018**, *6*, 5888–5895; b) M. Tian, R. Xing, J. Guan, B. Yang, X. Zhao, J. Yang, C. Zhan, S. Zhang, *Nano Lett.* **2021**, *21*, 5158–5166.

[21] a) N. Bertrand, M. A. Gauthier, C. Bouvet, P. Moreau, A. Petitjean, J. C. Leroux, J. Leblond, *J. Controlled Release* **2011**, *155*, 200–210; b) L. P. H. Yang, S. J. Keam, *Drugs* **2009**, *69*, 919–942.

[22] T. Steiner, *Angew. Chem. Int. Ed.* **2002**, *41*, 48–76.

[23] S. Chen, Y. Ruan, J. D. Brown, J. Gallucci, V. Maslak, C. M. Hadad, J. D. Badjic, *J. Am. Chem. Soc.* **2013**, *135*, 14964–14967.

[24] L. Zhiquan, S. Polen, C. M. Hadad, T. V. RajanBabu, J. D. Badjic, *J. Am. Chem. Soc.* **2016**, *138*, 8253–8258.

[25] P. Valluruapalli, A. Sekhar, T. Yuwen, L. E. Kay, *J. Biomol. NMR* **2017**, *67*, 243–271.

[26] P. Vallurupalli, G. Bouvignies, L. E. Kay, *J. Am. Chem. Soc.* **2012**, *134*, 8148–8161.

[27] L. Avram, A. Bar-Shir, *Org. Chem. Front.* **2019**, *6*, 1503–1512.

[28] L. Avram, V. Havel, R. Shusterman-Krush, M. A. Iron, M. Zaiss, V. Sindelar, A. Bar-Shir, *Chem. Eur. J.* **2019**, *25*, 1604.

[29] a) L. Avram, A. D. Wishard, B. C. Gibb, A. Bar-Shir, *Angew. Chem. Int. Ed.* **2017**, *56*, 15314–15318; b) Y. Cohen, S. Slovak, L. Avram, *Chem. Commun.* **2021**, *57*, 8856–8884.

[30] C. C. Slack, J. A. Finbloom, K. Jeong, C. J. Bruns, D. E. Wemmer, A. Pines, M. B. Francis, *Chem. Commun.* **2017**, *53*, 1076–1079.

[31] C. Witte, V. Martos, H. M. Rose, S. Reinke, S. Klippel, L. Schroeder, C. P. R. Hackenberger, *Angew. Chem. Int. Ed.* **2015**, *54*, 2806–2810.

[32] S. Klippel, C. Freund, L. Schroeder, *Nano Lett.* **2014**, *14*, 5721–5726.

[33] A. Okur, L. Wickstrom, M. Layten, R. Geney, K. Song, V. Hornak, C. Simmerling, *J. Chem. Theory Comput.* **2006**, *2*, 420–433.

[34] R. R. Johnson, A. Kohlmeyer, A. T. C. Johnson, M. L. Klein, *Nano Lett.* **2009**, *9*, 537–541.

[35] R. Qi, G. Wei, B. Ma, R. Nussinov, *Methods Mol. Biol.* **2018**, *1777*, 101–119.

[36] J. W. Barnett, M. R. Sullivan, J. A. Long, D. Tang, T. Nguyen, D. Ben-Amotz, B. C. Gibb, H. S. Ashbaugh, *Nat. Chem.* **2020**, *12*, 589–594.

[37] Z. Yan, T. McCracken, S. Xia, V. Maslak, J. Gallucci, C. M. Hadad, J. D. Badjic, *J. Org. Chem.* **2008**, *73*, 355–363.

[38] C. G. Jones, M. W. Martynowycz, J. Hattne, T. J. Fulton, B. M. Stoltz, J. A. Rodriguez, H. M. Nelson, T. Gonen, *ACS Cent. Sci.* **2018**, *4*, 1587–1592.

[39] M. Enache, E. Volanschi, *Rev. Roum. Chim.* **2010**, *55*, 255–262.

[40] a) S. E. Border, R. Z. Pavlovic, L. Zhiquan, J. D. Badjic, *J. Am. Chem. Soc.* **2017**, *139*, 18496–18499; b) A. Soldevilla, A. G. Griesbeck, *J. Am. Chem. Soc.* **2006**, *128*, 16472–16473; c) K.-D. Warzecha, H. Goerner, A. G. Griesbeck, *J. Phys. Chem. A* **2006**, *110*, 3356–3363; d) M. Oelgemoller, W. H. Kramer, *J. Photochem. Photobiol. C* **2010**, *11*, 210–244.

[41] a) R. Z. Pavlovic, S. E. Border, Y. Li, X. Li, J. D. Badjic, *Chem. Commun.* **2020**, *56*, 2987–2990; b) S. E. Border, R. Z. Pavlovic, Z. Lei, M. J. Gunther, H. Wang, H. Cui, J. D. Badjic, *Chem. Commun.* **2019**, 1987–1990.

[42] a) L. Xue, M. Zhang, G. Li, J. Cao, H. Yao, *Green Chem. Lett. Rev.* **2021**, *14*, 395–403; b) Y. Liu, M. Wei, Y. Hu, L. Zhu, J. Du, *Sens. Actuators B* **2018**, *255*, 544–551; c) A. A. Hamad, R. Ali, S. M. Derayea, *RSC Adv.* **2022**, *12*, 7413–7421; d) H. Yao, M. Zhang, W. Zeng, X. Zeng, Z. Zhang, *Spectrochim. Acta Part A* **2014**, *117*, 645–650.

[43] E. E. Patton, L. I. Zon, D. M. Langenau, *Nat. Rev. Drug Discovery* **2021**, *20*, 611–628.

[44] R. J. Andrade, N. Chalasani, E. S. Björnsson, A. Suzuki, G. A. Kullak-Ublick, P. B. Watkins, H. Devarbhavi, M. Merz, M. I. Lucena, N. Kaplowitz, G. P. Aithal, *Nat. Rev. Dis. Primers* **2019**, *5*, 58.

[45] A. Pastornicka, S. Rybarova, S. Drahosova, J. Mihalik, A. Krehel'ova, A. Pavliuk-Karachevtseva, I. Hodorova, *Int. J. Mol. Sci.* **2021**, *22*, 6363.

[46] K. Fukushima, M. Momose, C. Kondo, T. Higuchi, K. Kusakabe, N. Hagiwara, *Nucl. Med. Biol.* **2010**, *37*, 1005–1012.

[47] Deposition Number(s) 2261520 (for **1**) and 2179641 (for **1**) contain(s) the supplementary crystallographic data for this paper. These data are provided free of charge by the joint Cambridge Crystallographic Data Centre and Fachinformationszentrum Karlsruhe Access Structures service.

Manuscript received: October 13, 2023
Accepted manuscript online: October 18, 2023
Version of record online: ■■, ■■

RESEARCH ARTICLE

Deep-cavity baskets are novel, accessible, modular, and biocompatible hosts. With intriguing conformational dynamics, assembly characteristics and great capacity to bind anticancer drug mitoxantrone, deep-cavity baskets hold promise for developing antidotes as a countermeasure against a broad range of aromatic toxicants in complex biological systems.

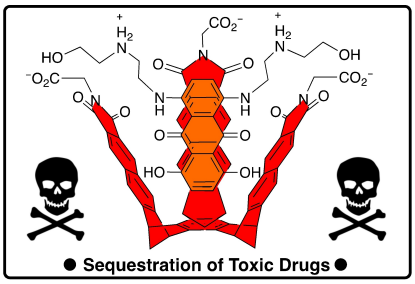

*R. Z. Pavlović, T. J. Finnegan, A. Metlushko, Dr. A. L. Hansen, Dr. C. A. Waudby, X. Wang, Dr. N. Hoefer, Prof. D. W. McComb, Prof. A. Pavić, N. Plackić, J. Novaković, J. Bradić, Prof. N. Jeremić, Prof. V. Jakovljević, Prof. B. Šmit, S. Matić, M. A. Alvarez-Saavedra, Prof. I. Čapo, Dr. C. E. Moore, Prof. S. I. Stupp, Prof. J. D. Badjić**